The Influence of Open Circuit Potential on Electrode Dynamics

Journal of The Electrochemical Society, 2025 **172** 090524
1945-7111/2025/172(9)/090524/10/$40.00

The Influence of Open Circuit Potential on Electrode Dynamics

Pierfrancesco Ombrini, Alexandros Vasileiadis, and Marnix Wagemaker[z]

Department of Radiation Science and Technology, Delft University of Technology, Delft 2629JB, The Netherlands

Phase separation, inducing a miscibility gap and non-monotonic open-circuit potential (OCP), is typical for widespread Li-ion battery electrodes such as $LiFePO_4$, $Li_4Ti_5O_{12}$ and Graphite. Although particle-scale effects of phase separation are well documented, its influence on transport-limited, porous electrodes remains largely overlooked. Here we embed physically consistent non-monotonic OCP profiles in a simplified Doyle–Fuller–Newman framework to compare their behavior against that of solid-solution materials with monotonic OCPs. Our findings provide deeper and general understanding of the different electrode ensemble behavior of solid solution (monotonic OCP) and phase separating (non-monotonic OCP) electrode materials, demonstrating why larger miscibility gaps are associated with decreasing rate capabilities and electrode utilization, amplifying local current heterogeneity and electrolyte depletion. By contrast, simulations employing conventional flat, fitted OCPs mask these effects and overpredict performance—particularly under dynamic cycling protocols such as galvanostatic intermittent titration (GITT). Our results reveal why accounting for realistic OCPs is essential for reliable modelling of high-loading electrodes, providing fundamental understanding and guidance for model-driven design and control of next-generation batteries.
 [DOI: 10.1149/1945-7111/ae01df]

Manuscript submitted June 30, 2025; revised manuscript received August 11, 2025. Published September 17, 2025.

Modeling electrodes for design and protocol optimization is necessary to advance both experimental research and commercial battery applications.[1,2] These models must be meticulously adapted to the properties of the active materials, and reflect their intrinsic thermodynamics, with phase separation being a critical yet often overlooked aspect. Conventional layered oxides, such as $LiCoO_2$ (LCO) and $LiNi_xMn_yCo_{1-x-y}O_2$ (NMC), undergo lithiation and delithiation as single-phase solid solutions, where ions and vacancies uniformly mix at all ionic concentrations.[3] In contrast, numerous prominent materials for Li-ion and Na-ion batteries—including $LiFePO_4$ (LFP),[4–7] $LiMn_xFe_{1-x}PO_4$ (LMFP),[8,9] $Li_4Ti_5O_{12}$ (LTO),[10] graphite,[11–13] $Na_3V_2(PO_4)_3$ (NVP),[14] and Prussian blue analogues (PB)[15]—exhibit a thermodynamic propensity to phase separate into ion-rich and ion-poor regions. This phase separation leads to a *miscibility gap*, preventing the material from achieving equilibrium across certain compositional ranges. For example, an LFP particle under equilibrium conditions can only be composed of two phases, having a filling fraction below ∼0.15 or above ∼0.85.[16–18] This phase separation behavior manifests as flat voltage plateaus and thermodynamic hysteresis, characterized by a persistent (small) voltage gap between charging and discharging even under equilibrium conditions.[19–21] Such phenomena directly influence key aspects of electrochemical performance, including energy efficiency, rate capability, and cycle life. Consequently, accurately modeling and optimizing battery performance necessitates addressing the effects of phase separation.

Significant advancements have been made in simulating the phase separation kinetics of both individual particles and particle ensembles. Depending on particle size and material diffusivity, particles may be categorized as either reaction-limited (charge transfer) or diffusion-limited (ion diffusion through the electrode particle).[22] For instance, LFP is generally synthesized with nanoscale particles to minimize diffusion length and enhance the surface-to-volume ratio, rendering it reaction-limited.[4] Phase-field models, such as Allen-Cahn reaction (ACR) model, have been developed to describe and predict the appearance or suppression of phase separation in single primary particles under varying current conditions.[16,17,23,24] In these cases, the model neglects the diffusion limitations and focus its attention on the heterogenous surface reaction kinetics.[23] Conversely, graphite, which is often utilized in larger particle sizes, typically exhibits diffusion-limited behavior.[12,13,25] In this case, Cahn-Hilliard reaction (CHR) models[7,10,26] effectively characterize the phase separation kinetics and predict concentration gradients along the particle's radius. Modeling the energy penalties associated with these gradients is necessary for estimating surface concentrations and thus improving the prediction of lithium plating risks and reaction kinetics.[11,27] Moreover, the electrochemical response of such systems can deeply vary when compared to similar electrodes that do not phase separate, misleading the interpretation of experimental and simulated results if the CHR dynamics is not considered.[7,10,28]

While modeling and understanding single-particle kinetics is integral to material engineering, the collective dynamics of multi-particle systems within an electrode play a decisive role in determining its overall performance.[20,29] Phase-separating electrodes exhibit distinct population kinetics due to the presence of an energy barrier for the nucleation of the secondary phase. Even under uniform electrochemical conditions, particle reactions occur heterogeneously. Certain particles, either due to smaller size or stochastic thermal fluctuations, nucleate first and dominate the reaction.[29] Consequently, the system evolves via particle-by-particle sequential reaction. At higher currents, more particles are utilized to sustain the reaction, increasing number of active particles.[20] These studies underscore the necessity of precise particle-scale models to properly assess the collective behavior. Nevertheless, they primarily focused on ultra-thin electrodes where the particles experience homogenous ionic and electronic potentials and dominant effects arise from interparticle dynamics rather than electrolyte polarization.

In practical applications, high-loading electrode behavior ($>4\ mAh\ cm^{-2}$) is predominantly governed by electrolyte and electronic transport.[30,31] Therefore, electrode design efforts prioritize minimizing tortuosity and optimizing active material volume fractions.[2] Semiconductor-based materials, like LFP, exhibit lower electronic conductivity and solid-state diffusivity than transition metal oxides like LCO or NMC.[32] As a result, these electrodes require additional engineering measures, including carbon coatings, nanoscale particle design, and conductive additives.[33] These morphological and compositional strategies aim to overcome intrinsic charge and ion mobility limitations. This added complexity in structure and transport behavior, in turn, affects how phase separation manifests and evolves within the electrode.[30,31] Consequently, the role of phase separation in determining the performance of thick electrodes remains difficult to isolate, resulting in transport kinetics studies that focus microstructural properties[2,34] without considering thermodynamic effects.[30]

To gain insight in the role of phase separation, inducing a non-monotonic OCP, we simulate an idealized, one-dimensional porous electrode composed of reaction-limited particles of identical size. Each particle is assumed to remain homogeneous, hence solid-state diffusion cannot obscure electrode-scale phenomena. Throughout all simulations, kinetic parameters are held constant, while equilibrium

[z]E-mail: m.wagemaker@tudelft.nl

thermodynamic properties are varied. Specifically, we use the regular solution model[8,35–37] to calculate each particle's free energy landscape under different ion–vacancy interaction energies. As the repulsion between ions and vacancies increases, the material's OCP—computed from its homogeneous chemical potential—transitions from a monotonic to a strongly non-monotonic profile. This framework enables us to uncover the role of depth-wise inter-particle phase separation in governing reaction localization, electrode utilization, and electrolyte transport under both constant-current (CC) and galvanostatic intermittent titration (GITT) protocols.

Notably, this thermodynamic framework naturally reproduces the voltage plateaus and hysteresis characteristic of materials with a miscibility gap. In contrast, conventional models often fit experimental OCPs of materials like LFP and LTO using voltage curves obtained from slow (C/100) lithiation and delithiation. This approach yields two artificially flat OCPs[38]—one for charge and one for discharge—and requires empirical approximations to interpolate between them during dynamic cycling.[39] In this context, we compare the physically consistent model to the flat-plateau approximation, quantifying the errors that arise when phase-separating materials are represented using monotonic OCP profiles.

The remainder of the paper is organized as follows. In the first part, we introduce the theoretical framework, describing the OCP model and its derivation from free energy and the parameter Ω, which controls phase-separation tendency and miscibility gaps. In the second part, we analyze the system under constant-current (CC) conditions, evaluating its behavior across different OCP profiles. The third part explores dynamic response under a galvanostatic intermittent titration technique (GITT) protocol. In the fourth part 4, we investigate the influence of kinetic parameters, particularly the characteristic diffusion and reaction times, and their effects on reaction localization and electrode utilization. In the last section, we compare the physically consistent OCP model to a conventional flat OCP approximation, highlighting differences in both behavior and implementation under CC and GITT conditions. We conclude by summarizing the key findings and discussing broader implications for phase-separating electrode materials and model-based electrode design.

Theory

From the free energy to the open circuit potentials.—To generalize this study and capture a continuous range of materials differing only in their OCP and phase transition characteristics, we adopt a general formulation derived from thermodynamic principles. In this framework, the OCP is directly related to the free energy of the system. Specifically, the homogeneous free energy landscape $g(\tilde{c}_s)$ can be modeled using regular solution theory[8,35–37]:

$$g(\tilde{c}_s) = -eV_0\tilde{c}_s + k_BT\left[\tilde{c}_s \ln \tilde{c}_s + (1-\tilde{c}_s)\ln(1-\tilde{c}_s)\right] + \Omega\,\tilde{c}_s(1-\tilde{c}_s) \quad [1]$$

Where V_0 is the reference potential, $\tilde{c}_s$ is the normalized solid particle concentration ($\tilde{c}_s = c_s/c_{\max}$), k_B is the Boltzmann constant, e is the electron charge, and T is the temperature. The main factor regulating the free energy is Ω, called the regular solution parameter. It controls the interaction between inserted species and vacancies, so that when $\Omega < 0$ an attractive interaction between ions and vacancy is considered, while $\Omega > 0$ indicates a repulsive interaction. If $\Omega = 0$ the system is an ideal solution where the mixing free energy is solely regulated by the entropic contribution and the minimum of $g(\tilde{c}_s)$ coincides with the maximum mixing at $\tilde{c}_s = 0.5$. This case is thus considered a *solid solution*. At $\Omega = 2\,k_BT$ the entropic and enthalpic energies compensate each other, leading to a flat free energy landscape (Fig. 1a). If Ω exceeds this threshold, the free energy presents two minima, signifying that the system's energy is minimized by a combination of two phases, each of them having concentration corresponding with the minima (Fig. 1a). This condition leads to a thermodynamic drive for *phase separation*. Increasing Ω leads to diverging minima, increasing the miscibility gap.

The open circuit potential can be derived from the regular solution free energy:

$$U(\tilde{c}_s) = -\frac{1}{e}\frac{dg}{d\tilde{c}_s} = V_0 - \frac{k_BT}{e}\ln\frac{\tilde{c}_s}{1-\tilde{c}_s} - \frac{\Omega}{e}(1-2\tilde{c}_s) \quad [2]$$

The effect of Ω on the OCP is shown in Fig. 1b. When $\Omega > 2k_BT$ the OCP results *non-monotonic*. This corresponds to phase-separating materials, whereas for $\Omega < 2k_BT$ the OCP decreases monotonically with increasing filling fraction, similarly to the behavior of transition metal oxides such as LCO and NMC.[40,41] Although this simplified representation does not capture all the nuances of real materials, it effectively models key characteristics observed in materials such as LFP,[7,16] LMFP,[8] LTO,[10] etc. Moreover, advanced models that reconstruct the full free energy landscape have validated this approach.[16] It is important to note that the total free energy of a non-homogeneous particle, and consequently its OCP, also depends on additional factors such as boundary energy penalties and chemo-mechanical effects.[5,6,23] However, for the sake of clarity and the focus on the impact of the OCP, in this work these factors are neglected, thus assuming the particles remain homogeneous.

Within this theoretical framework, the existence of multiple minima in the free energy landscape, leading to phase separation, is consistently linked to miscibility gaps, voltage plateaus, and thermodynamic hysteresis. In fact, while the OCP of a single particle can be non-monotonic, the collective behavior of multiple particles leads to the experimentally observed voltage plateaus and hysteresis. During (de)insertion, the particles rapidly equilibrate their chemical potential to the global maximum (or minimum), effectively smoothing out the non-monotonic features.[19]

Aside from the local inter-particle phase separation behavior, the insertion dynamics of a transport-limited electrode are inherently influenced by the monotonicity of the OCP, as illustrated in Fig. 2. Under near-equilibrium conditions, a thin, reaction-limited electrode composed of phase-separating particles would react heterogeneously due to thermal fluctuations and particle size differences.[20,29] In contrast, in transport-limited electrodes operating under dynamic conditions, a non-monotonic OCP induces depth-wise heterogeneous reactions.

For the case of non-monotonic OCP (phase-separating material in Fig. 2), initially, transport-induced potential drops allow only the region near the separator–electrode interface to exceed the insertion threshold, while deeper sections remain inactive. As insertion progresses in the reactive region, the increasing solid-phase concentration raises the particle surface potential, which in turn enhances the local overpotential and accelerates the reaction. This autocatalytic mechanism concentrates the reaction within a narrow zone of the electrode. Once the reacting particles in this zone complete insertion, the reaction front advances further into the electrode (second step of Fig. 2). Owing to the symmetric shape of the OCP, this phenomenon occurs during both insertion and de-insertion in phase-separating materials, driving the system toward a phase-separated state.

In contrast, monotonically decreasing OCPs (solid-solution material in Fig. 2) are less susceptible to this localization. As the local solid-phase concentration increases, the particle potential decreases, reducing the overpotential and thus the reaction rate. This autoinhibitory effect, combined with the absence of a potential threshold, enables the entire electrode to react more uniformly. Although the reaction still initiates near the separator, the continuous variation in overpotential leads to a more homogeneous current distribution.

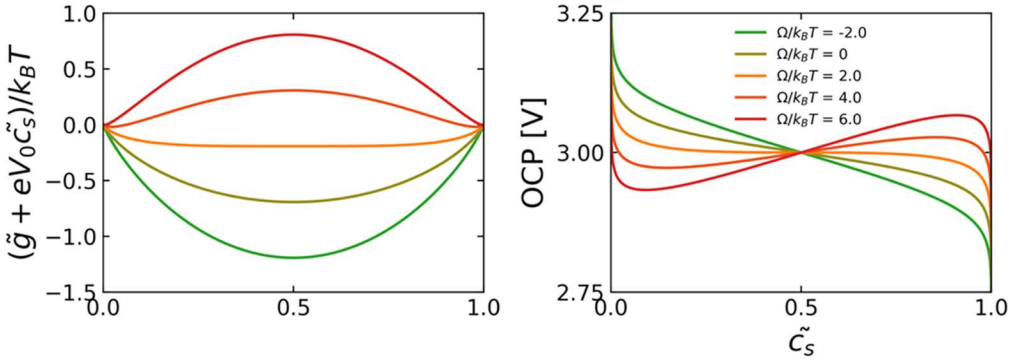

Figure 1. From the free energy to the OCP. (a) Free energy of the regular solution model at various Ω s. (b) Open circuit potential at various Ω s in case of $V_0 = 3\ V$.

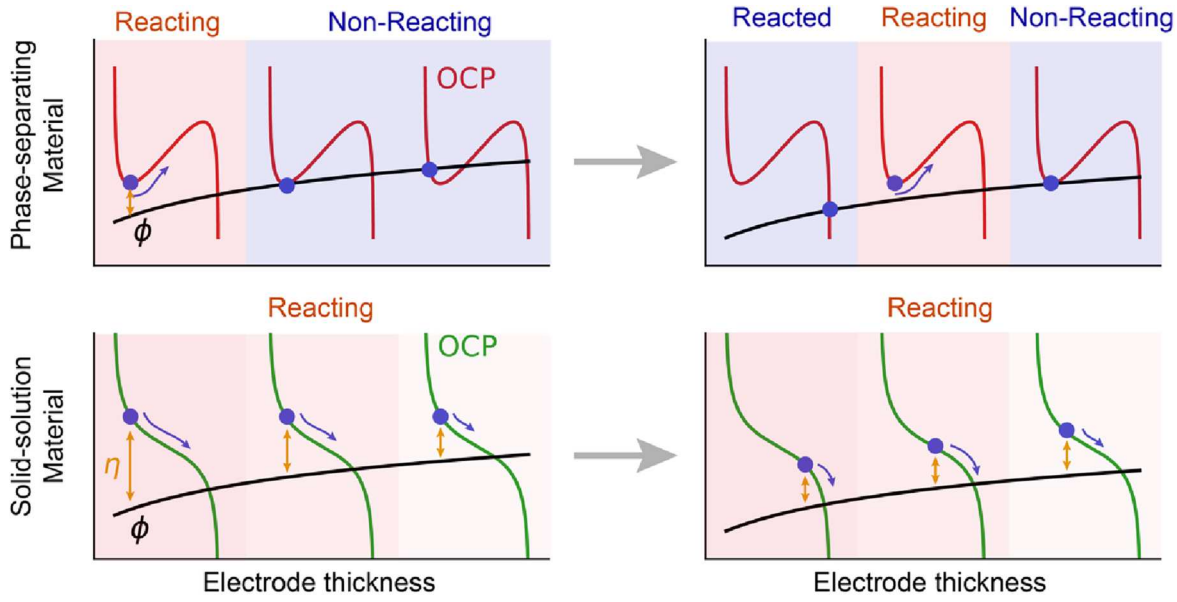

Figure 2. Schematic representation comparing the electrode dynamic of a solid solution material and a phase-separating material during an insertion process. The separator is assumed to be on the left of the electrode, while the current collector is on the right. The OCP of the phase-separating material is shown in red, while the OCP of the solid solution material is in green. The potential difference between electron-conducting and ion-conducting phases (ϕ), sloping due to transport limitations, is represented in black. The reaction overpotential (η), leading to an insertion process, is depicted in yellow.

In this illustrative example, we neglected electrolyte concentration variations, so the localized reaction arises solely from changes in particle potential. However, as shown in the results section, non-monotonic OCPs also significantly affect electrolyte dynamics, further enhancing reaction localization.

Model's equations.—To investigate these effects, we employ a simplified one-dimensional porous electrode model of a homogenous electrode, hereby described. In this model, a porous electrode, of length L, is considered filled with a binary monovalent dilute electrolyte of concentration c_e, having equal diffusivities of positive and negative ions ($D_- = D_+$), so that the ambipolar diffusivity (D_{amb}) coincides with D_+ and the transference number is 1/2. Given a porosity ε and a tortuosity τ_e the governing equation for the electrolyte concentration results[35,36,42–44]

$$\varepsilon\frac{dc_e}{dt} = \frac{d}{dx}\left(\frac{\varepsilon}{\tau_e}D_+\frac{dc_e}{dx}\right) + \frac{a\,j(x)}{2\,F} \qquad [3]$$

where a is the specific reactive surface area (m^2/m^3), and the local current density $j(x)$ changes along the domain axis x, depending on the local reaction rate. In this work we neglect the concentration dependence of the electrolyte diffusivity and assume a tortuosity equal to one. Neglecting also the electric losses along the electrode's thickness, we can define an electrode potential difference ϕ which will be regulated by the charge conservation in the electrolyte:

$$\frac{d}{dx}\left(\kappa\frac{d\phi}{dx}\right) = aj(x) \qquad [4]$$

with the electrolyte conductivity κ being the one of a dilute electrolyte

$$\kappa = 2\frac{F^2}{RT}\frac{\varepsilon}{\tau_e}D_+c_e \qquad [5]$$

where, F is the Faraday constant and R the gas constant, and the concentration term disappear since $D_+ = D_-$. The electrode potential difference ϕ is conventionally defined as the difference between the solid phase potential ϕ_s and the electrolyte potential ϕ_e.[42] In this work, since the ohmic losses in the solid phase are assumed negligible, we can use a single variable $\phi = \phi_s - \phi_e$. Moreover, neglecting the presence of separator or resistance between the current collector and the active material, the output voltage is $V = \phi(x = 0)$ and its initial condition, depends on the initial solid concentration is $V(t = 0) = U(\tilde{c}_s(t = 0))$. The local reaction rate is expressed in

using the symmetric Butler-Volmer kinetics ($\alpha = 1/2$):

$$j = k_0 \sqrt{\tilde{c}_e} \sqrt{\tilde{c}_s(1-\tilde{c}_s)} \left[e^{\frac{F}{RT}\frac{\eta}{2}} - e^{-\frac{F}{RT}\frac{\eta}{2}} \right] \quad [6]$$

so that it depends on the exchange current density k_0 (A/m^2), the normalized electrolyte concentration $\tilde{c}_e = c_e/c_e(t=0)$, the normalized particle concentration $\tilde{c}_s$, and the reaction overpotential

$$\eta = \phi - U(\tilde{c}_s) \quad [7]$$

Finally, the particles are simulated as homogenous and using a zero-dimensional approximation, so their concentration a evolves as

$$\varepsilon_s \frac{d\tilde{c}_s}{dt} = -\frac{a\, j}{c_{\max}\, F} \quad [8]$$

where ε_s is the active material volume fraction, here coinciding with $1-\varepsilon$, since no conductive domains or binders are considered. We scale the imposed current density and the boundaries (I) by the C-rate (where C-rate = 1 indicates the full (dis)charge of the electrode in 1 h):

$$I = c_{\max} F \varepsilon_s L C_{rate} \quad [9]$$

So that the boundary conditions result from assuming no ionic flux at the outer boundary (current collector):

$$\left.\frac{dc_e}{dx}\right|_{x=L} = 0 \quad [10]$$

$$\left.\frac{d\phi}{dx}\right|_{x=L} = 0 \quad [11]$$

and imposed current at the inner boundary, i.e. considered as an infinite ionic source:

$$\varepsilon \left.\frac{dc_e}{dx}\right|_{x=0} = -\frac{I\tau_e}{2\, F\, D_+} \quad [12]$$

$$\left.\frac{d\phi}{dx}\right|_{x=0} = \frac{I}{\kappa(x=0)} \quad [13]$$

While more advanced electrochemical descriptions are available,[36,42,44] the presented model is built to only focus on two limiting factors: electrolyte transport and the reaction kinetics at the active material-electrolyte interface. These two processes define the overall behavior of the idealized electrode and can be characterized by two fundamental timescales:

$$\text{Reaction time: } \tau_R = \frac{\varepsilon_s c_{\max} F}{a k_0} \quad [14]$$

$$\text{Diffusion time: } \tau_D = \frac{\tau_e L^2}{\varepsilon\, D_+} \quad [15]$$

These characteristic timescales are then compared to the charging timescale, τ_C, defined based on the C-rate:

$$\tau_C = \frac{L c_{\max}\, F \varepsilon_s}{I} = \frac{1}{C_{rate}} \quad [16]$$

The ratio of these timescales determines the dominant transport mechanism. For instance, when $\tau_C < \tau_D$, the diffusion process is slower than the insertion, leading to the development of concentration gradients. Conversely, when $\tau_C < \tau_R$, t the reaction kinetics become the limiting factor, significantly increasing the overpotential. To further quantify the distribution of the reaction within the electrode, we define a normalized current density $\tilde{j}$:

$$\tilde{j} = \frac{a\, L\, j}{I} \quad [17]$$

So that, in a perfectly uniform electrode, the average volumetric current density (I/L) coincides with the local volumetric current density ($a\, j$), resulting in $\tilde{j} = 1$. However, non-uniform insertion rates increase $\tilde{j}$, indicating the formation of localized reaction and the presence of current hotspots. A summary of the model's equations is provided in Table I.

Table I. Summary of the governing equations, boundary conditions and assumptions.

Variable	Governing equations	Boundary conditions	Assumptions
Electrolyte concentration c_e	$\varepsilon \frac{dc_e}{dt} = \frac{d}{dx}\left(\frac{\varepsilon}{\tau_e} D_+ \frac{dc_e}{dx}\right) + \frac{a\, j(x)}{2\, F}$	$\varepsilon \left.\frac{dc_e}{dx}\right\|_{x=0} = -\frac{I\tau_e}{2\, F\, D_+}$ $\left.\frac{dc_e}{dx}\right\|_{x=L} = 0$	No separator Monovalent dilute electrolyte $D_+ = D_-$ D_+ independent on concentration
Electrode potential difference ϕ	$\frac{d}{dx}\left(\kappa \frac{d\phi}{dx}\right) = aj(x)$	$\left.\frac{d\phi}{dx}\right\|_{x=0} = \frac{I}{\kappa(x=0)}$ $\left.\frac{d\phi}{dx}\right\|_{x=L} = 0$	Negligible ohmic losses in the solid phase Dilute electrolyte conductivity: $\kappa = 2\frac{F^2}{RT}\frac{\varepsilon}{\tau_e} D_+ c_e$
Normalized solid concentration $\tilde{c}_s$	$j = k_0 \sqrt{\tilde{c}_e} \sqrt{\tilde{c}_s(1-\tilde{c}_s)} [e^{\frac{F}{RT}\frac{\eta}{2}} - e^{-\frac{F}{RT}\frac{\eta}{2}}]$ $\eta = \phi - U(\tilde{c}_s)$ $U(\tilde{c}_s) = V_0 - \frac{k_B T}{e} \ln \frac{\tilde{c}_s}{1-\tilde{c}_s} - \frac{\Omega}{e}(1-2\,\tilde{c}_s)$ $\varepsilon_s \frac{d\tilde{c}_s}{dt} = -\frac{a\, j}{c_{max}\, F}$		Negligible solid diffusion limitations Uniform reaction on the particles surface Identical size OCP described by regular solution theory

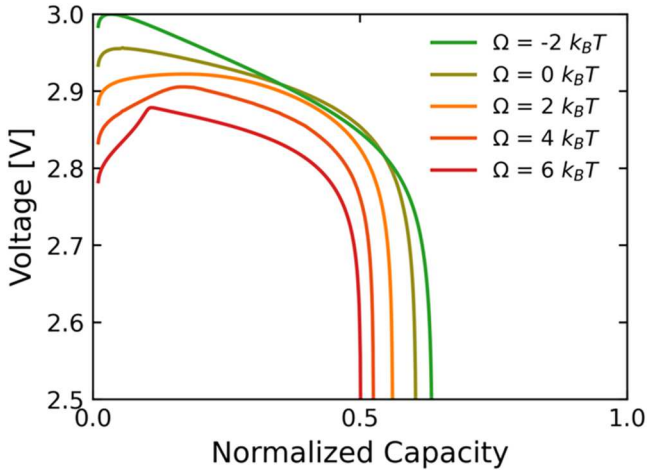

Figure 3. Comparison between the constant current responses of the model at varying Ωs. The various colors indicate different values of Ω.

The model was implemented using the open-source software *PyBaMM*.[45] Specifically, the *BaseModel* class was extended to include the specified set of equations and boundary conditions and using the software we implemented 300 spatial discretization points. The time integration was performed using CasADi solver.[46]

Results

To evaluate the impact of varying Ω on electrode kinetics, we simulated an electrode where the characteristic timescales were set to be equal, i.e., $\tau_C = \tau_D = \tau_R$. The simulations were performed for an insertion process with an initial normalized concentration of $\tilde{c}_i = 0.01$. It is important to clarify the terminology used in conventional battery protocols. Typically, the discharge process refers to ion insertion into the positive electrode. Since this study presents a general analysis of an insertion process, and we set the average potential at $V_0 = 3$ V, we define our applied protocols as discharge. However, due to the symmetry of the open circuit potential (OCP) and reaction kinetics, the same results can be extended to the de-insertion process—corresponding to the charge of a positive electrode or the discharge of a negative electrode.

To account for differences in OCPs across simulations, we imposed a cutoff voltage based on the total overpotential, setting $V - U = -0.5V$. The electrode porosity was fixed at 0.5. A realistic example of such a system would be a half-cell discharging at a rate of 5 C (completing a full (dis)charge in 720 s) with an electrolyte diffusivity of $D_+ = 10^{-10}\mathrm{m^2s^{-1}}$, and an electrode of thickness of 190 μm. Moreover, to assure a negligible solid diffusion the electrode could composed by particles of 50 nm of radius ($a = 3{\cdot}10^7\mathrm{m^{-1}}$), having $k_0 = 4{\cdot}10^{-2}\mathrm{Am^{-2}}$. Using these parameters, we simulated two distinct cases: a constant current scenario and a galvanostatic intermittent titration protocol (GITT). We then proceeded to analyze the effects of varying τ_D and τ_R on electrode performance and kinetics, providing insight into how phase separation influences transport limitations and reaction localization.

Constant current protocol.—Figure 3 presents a comparison of the constant current responses of the model across different values of Ω. An unexpected result emerges: the properties of the open circuit potential (OCP) influence the capacity retention of the system. Despite identical discharge rates and electrode kinetic properties, higher values of Ω, corresponding to a stronger tendency for phase separation, lead to greater capacity losses. Notably, this effect is not limited to the transition from solid solution behavior ($\Omega < 2k_BT$) to phase-separating behavior ($\Omega > 2k_BT$) but rather persists as Ω increases continuously. Specifically, the initial potential drops are related to the reaction kinetics, where the lower exchange current density at lower solid concentrations increase the overpotential, and the utilized electrode surface scales with Ω.

The subsequent sloping voltage profile is instead related to the electrolyte transport, where the influence of OCP on kinetic performance can be understood by analyzing the evolution of key variables during the insertion process, as shown in Fig. 4. When comparing the limiting cases of $\Omega = -2k_BT$ and $\Omega = 6k_BT$, significant differences emerge. In the former case, the solid concentration $\tilde{c}_s$ remains uniform throughout the electrode, whereas in the latter case, it exhibits an abrupt transition, forming a strong concentration gradient (Figs. 4a, 4d). This depth-resolved phase separation is driven purely by the non-monotonic OCP. As in thin electrode phase separation occurs either between or within particles, in this transport-limited system it manifests along the electrode thickness.

This phenomenon is closely coupled with the evolution of electrolyte concentration $\tilde{c}_e$ (Figs. 4b, 4e). In the solid solution case, $\tilde{c}_e$ quickly stabilizes, reaching a quasi-steady-state early in the process and undergoing minimal changes throughout the reaction. Conversely, in the phase-separating case $\tilde{c}_e$ continues evolving during the entire insertion process. This difference arises due to variations in the local reaction rate, as illustrated in Figs. 4c and 4f. When the material undergoes phase separation, the local current density can be up to 20 times higher than the average value, leading to a highly localized reaction at the interface between reacted and unreacted regions.

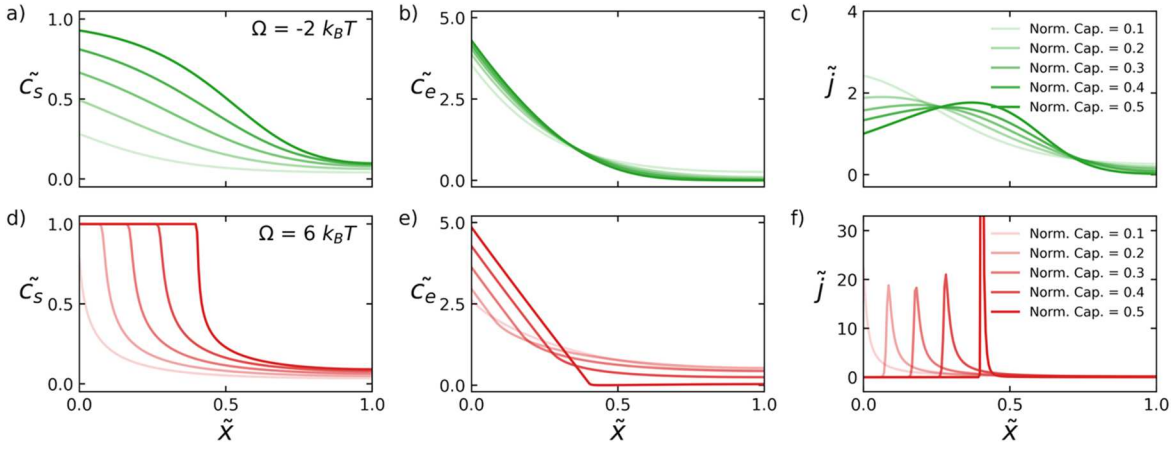

Figure 4. Evolution during the constant current protocol. Evolution of normalized solid concentration $\tilde{c}_s$ (a), (d), normalized electrolyte concentration $\tilde{c}_e$ (b), (e), and normalized volumetric current density $\tilde{j}$ (c), (f), during the constant current protocol along the normalized electrode thickness $\tilde{x} = x/L$. The green lines correspond to the case with $\Omega = -2k_BT$ while the red lines represent the case with $\Omega = 6k_BT$. Transparency indicates the corresponding normalized capacity.

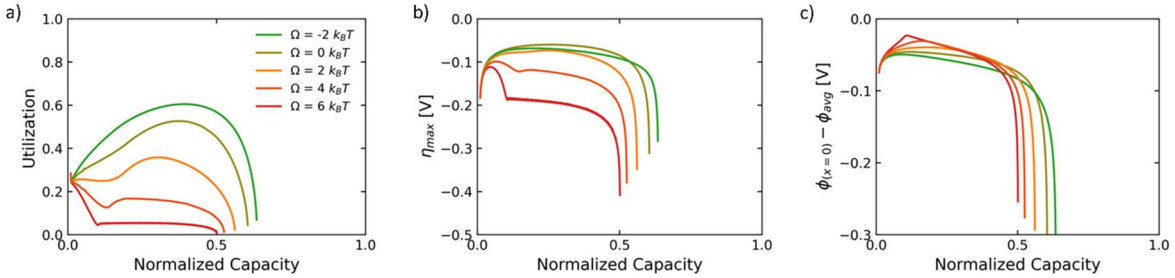

Figure 5. Evolution of utilization (a), maximum reaction overpotential (b) and transport overpotential (c) during the constant current protocol. The various colors indicate different values of Ω.

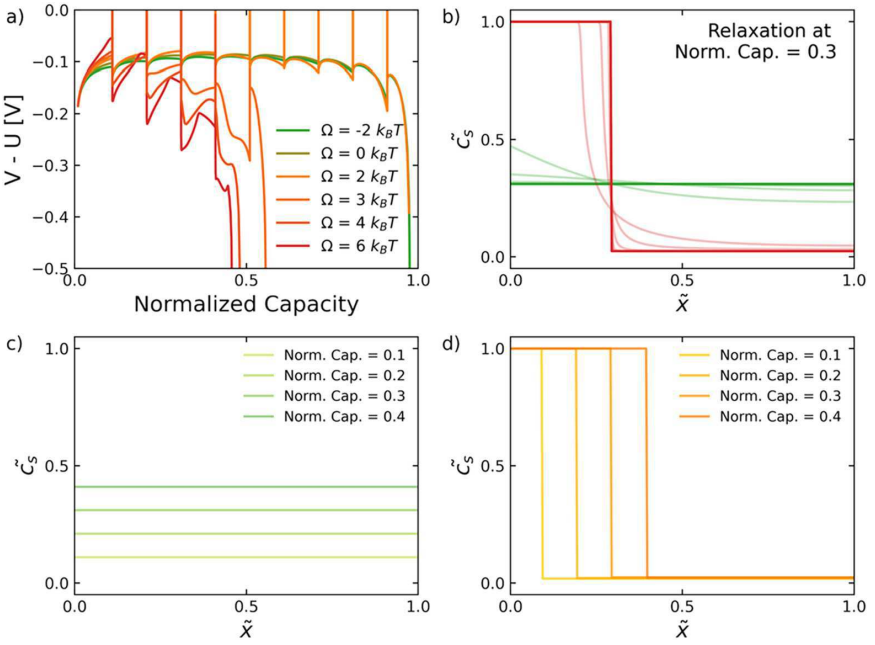

Figure 6. Evolution during the GITT protocol. (a) Evolution of the total overpotential (V—U) during the various pulses, plotted against the normalized capacity. (b) Relaxation of the normalized solid concentration after the third pulse along the normalized electrode thickness $\tilde{x}$. The green lines refer to the $\Omega = -2k_BT$ case, the red lines to the $\Omega = 6k_BT$ case. The transparent lines correspond to the result after the pulse and subsequent relaxation. The opaque line corresponds to the profile reached at the end of the relaxation process. (c), (d) Normalized depth-resolved solid concentration at various normalized capacities during the GITT protocol at the end of the relaxation, for the $\Omega = -2k_BT$ case (c) and the $\Omega = 6k_BT$ case (d).

This localized reaction leads to electrolyte depletion, which increases electrolyte polarization and ultimately reduces capacity retention. Additionally, higher local current densities correlate with increased overpotential and the onset of degradation mechanisms. These findings, in line with experimental results,[30] highlight the importance of accounting for phase-separation effects when designing electrodes and optimizing charging protocols for phase-separating materials.

Finally, we examine the evolution of key indicators during the reaction process.[47] The heterogeneous nature of the reaction at the electrode scale manifests as an increasing disparity between the imposed current density and the local current density. This effect can be quantified using the *utilization*, defined as:

$$Utilization = \frac{1}{\max \tilde{j}} \qquad [18]$$

In the case of a perfectly homogeneous current distribution, where $\tilde{j} = 1$ (i.e. $aj = J/L$), the utilization is equal to 1, indicating that the entire electrode volume participates in the reaction. However, when the current is localized, only a fraction of the electrode is actively utilized during the insertion process. Figure 5a presents the evolution of utilization over the discharge process, highlighting a striking contrast in the effective use of active material between phase-separating and solid solution materials. As the miscibility gap increases (i.e., with increasing Ω), utilization decreases significantly.

The consequences of this reduced utilization are evident in Figs. 5b and 5c, which show the evolution of the maximum reaction overpotential $\eta_{\max}$ and the transport overpotential $(\phi_{x=0} - \phi_{avg})$ as functions of Ω. The behavior of $\eta_{\max}$ reveals an initial decrease due to the increased exchange current density in the Butler-Volmer kinetics. However, in phase-separating cases, once the system surpasses the miscibility gap, $\eta_{\max}$ abruptly increases to overcome the nucleation barrier. As the reaction progresses, the need to activate particles located further from the ion source (separator) maintains this high overpotential until a reduction in c_e forces the system to reach the cutoff voltage.

The transport overpotential follows a different trend. In phase-separating systems, the presence of a reaction front near the separator

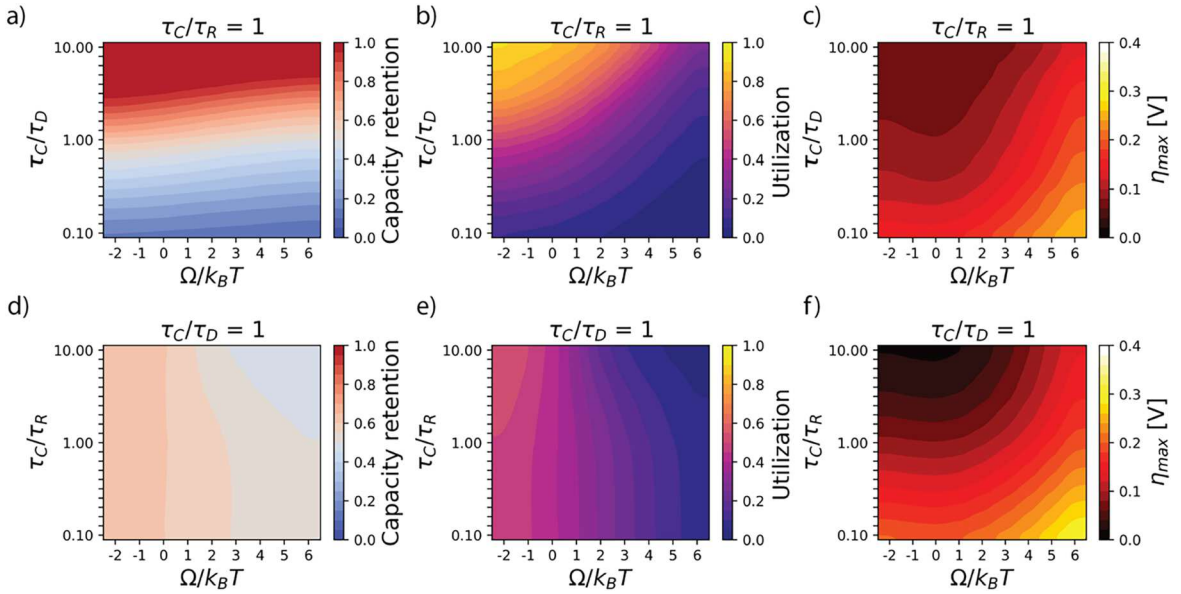

Figure 7. The effect of kinetic parameters on the constant current protocol. Capacity retention at varying kinetic ratios: τ_C/τ_D (a) and τ_C/τ_R (d). Mean utilization during the discharge at varying at varying τ_C/τ_D (b) and τ_C/τ_R (e). Maximum absolute value of the reaction overpotential during the discharge at varying at varying τ_C/τ_D (c) and τ_C/τ_R (f). Where $\tau_C = 1/C\_rate$, τ_D is the characteristic diffusion time along the electrode thickness and τ_R is the characteristic reaction time.

initially results in a lower transport overpotential compared to solid solution cases. However, as the reaction extends deeper into the electrode and electrolyte depletion becomes more pronounced, the transport overpotential in phase-separating cases eventually surpasses that of solid solution materials.

GITT protocol.—The presence of non-monotonic chemical potentials is also affecting the electrode dynamics during resting periods and subsequent current pulses. To establish its impact, we simulated a galvanostatic intermitted titration (GITT) protocol where the electrode was pulsed multiple times for a duration of $\tau_C/10$ and rested for $5\tau_D$, until the cutoff voltage was reached. As shown in Fig. 6a, while the constant current case exhibits only minor differences among OCPs (Fig. 3), the extracted capacity and overpotential in the GITT protocol are significantly affected by the OCP, and consequently, by phase separation dynamics. In the case of $\Omega \leqslant 2k_BT$, the total overpotential remains stable across multiple pulses. During the resting period, the solid concentration returns to a homogeneous and stable value (Figs. 6b–6c), ensuring that each pulse follows similar dynamics, governed primarily by the concentration dependence of reaction kinetics (Eq. 7). For $\Omega > 2k_BT$, however, the system reaches an equilibrium concentration profile composed of two distinct regions with strongly differing concentrations (Figs. 6b, 6d). The portion of the electrode near the separator equilibrates in a fully inserted state, while the remaining electrode volume becomes depleted. This pattern repeats with each pulse, resulting in a continuous reaction across the entire electrode for $\Omega \leqslant 2k_BT$ case (Fig. 6c), while for $\Omega > 2k_BT$ a narrow insertion front develops and propagates from the separator (Fig. 6d). This behavior arises as the system seeks to minimize its total free energy.

The consequences of this heterogeneous concentration profile become apparent in subsequent pulses. In phase-separating materials ($\Omega > 2k_BT$), since the system reaches thermodynamic equilibrium as separated into two distinct phases, the electrolyte must transport ions over a greater distance to reach the non-reacted region, and the total amount of active material available for the reaction decreases during subsequent pulses. As the protocol progresses, these effects lead to an overpotential buildup that persists despite the resting periods. In other words, the electrode retains a memory, meaning that the concentration inhomogeneities formed during prior pulses do not dissipate during open circuit rest, further influencing the response of subsequent cycles. We also show how this effect is proportional to Ω, i.e. proportional to the miscibility gap: the wider the concentration difference between the two phases, the greater the remaining heterogeneity after relaxation. These findings complement previously reported results, where various protocols applied to phase-separating materials show path-dependencies[7,18,48,49] and unusual features,[28] strengthening the need for physically consistent modeling of phase separating materials.

The effect of kinetic parameters.—Having established the significant impact of the miscibility gap on electrode kinetics and performance, we now examine the effect of varying the ratio between characteristic timescales. As expected, capacity retention improves when the diffusion time is reduced, such as in the case of a thinner electrodes, slower discharging or improved ionic diffusivity. This trend is observed consistently across all values of Ω (Fig. 7a). A similar effect is seen in average utilization, which exhibits a strong dependence on both diffusion time and Ω (Fig. 7b). Additionally, as τ_D increases, the local reaction rate becomes more homogeneous, while its overall magnitude increases with larger Ω (Fig. 7c).

More unexpectedly, in the case of phase separating materials ($\Omega > 2k_BT$), a reduction in reaction time τ_R (decrease in charge transfer resistance) leads to a decrease in capacity retention (Fig. 7d), indicating that improving charge transfer kinetics can actually reduce the extracted capacity at the same rates. This counterintuitive behavior can be explained by the sharp decline in utilization observed for lower τ_R (Fig. 4e). When deviations from the equilibrium potential occur, local reaction kinetics increase significantly, promoting stronger inhomogeneous reactivity. This results in a more localized reaction front (Fig. 4f), which rapidly depletes the electrolyte near the reaction sites, ultimately causing a sudden voltage drop.

Comparison between physically derived and fitted OCPs.—Finally, we compare the results obtained using the physics-based OCP with those from the conventional fitted flat voltage plateau.[38] For $\Omega = 4k_BT$, the resulting energy barrier is consistent with values typically observed for LFP.[17] Under constant current conditions, the voltage profiles obtained from both approaches appear comparable (Fig. 8a). This apparent similarity is likely the reason why the fitted approach remains widely used.

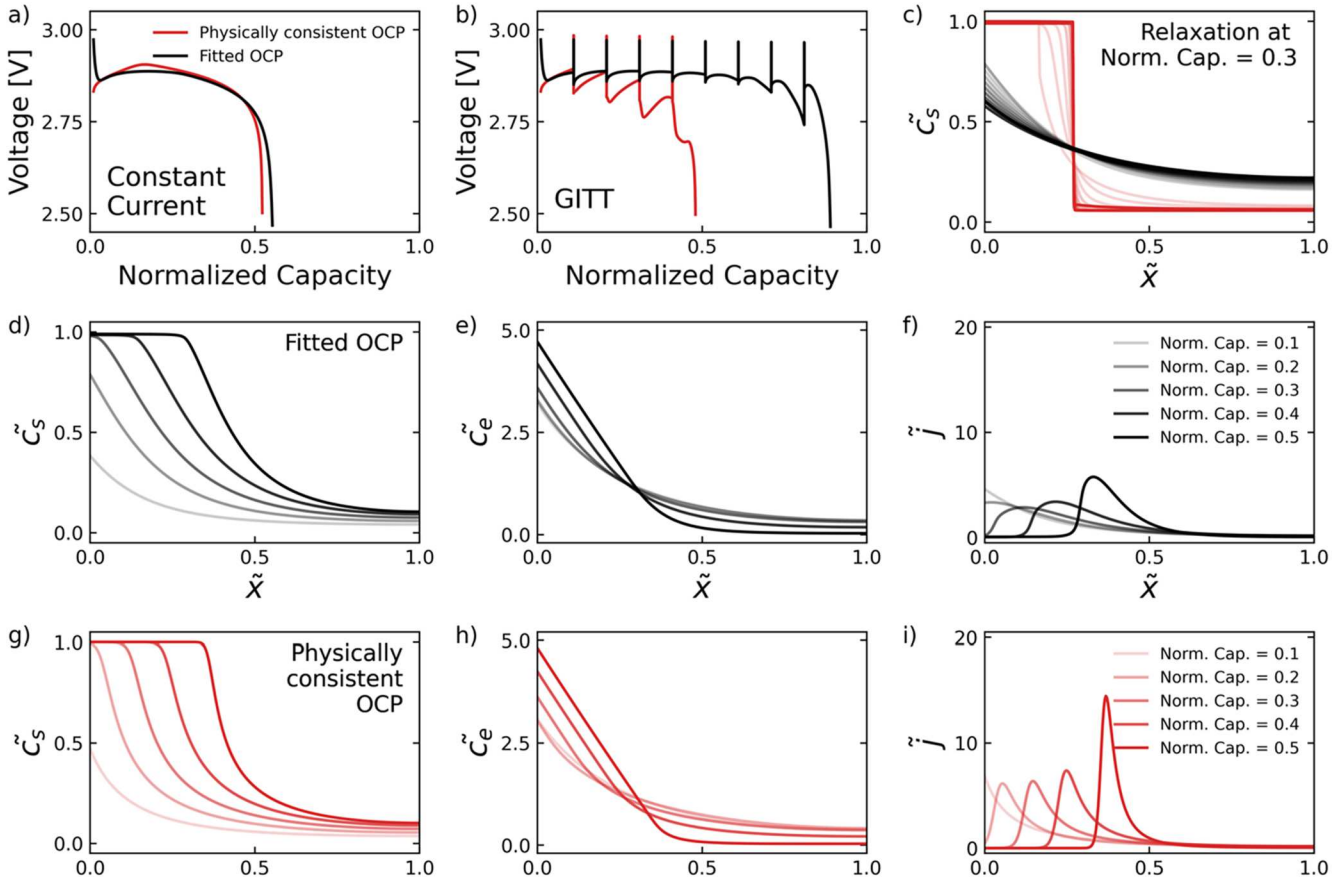

Figure 8. Comparison between physically-consistent non-monotonic OCP and fitted flat OCP. Voltage responses of the constant current protocol at $\tau_C = \tau_D = \tau_R$ (a). Voltage responses to the GITT protocol (b). Relaxation of the normalized solid concentration after the third pulse along the normalized electrode thickness $\tilde{x}$. The transparent lines correspond to the result after the pulse and subsequent relaxation. The opaque line corresponds to the profile reached at the end of the relaxation process (5 τ_D) (c). Kinetic evolution of normalized solid concertation $\tilde{c}_s$ (d), (g), normalized electrolyte concertation $\tilde{c}_e$ (e), (h), and normalized volumetric current density $\tilde{j}$ (f), (i), during the constant current protocol along the normalized electrode thickness $\tilde{x}$. The black lines correspond to the case flat OCP case, while the red lines represent the physics-based case with $\Omega = 4k_BT$. Transparency indicates the corresponding normalized capacity.

However, while the constant current response may seem indistinguishable, the underlying electrode kinetics differ significantly. When applying the GITT protocol, a clear discrepancy emerges between the physics-based and fitted models (Fig. 8b). The physically consistent model naturally incorporates the thermodynamic drive for phase separation, preventing the electrode from fully relaxing during the 5 τ_D resting period. As a result, the system enters each subsequent pulse in a heterogeneous state, where the region near the separator becomes fully intercalated, while the area further away remains depleted (Fig. 8c). Consequently, during the next pulse, the reaction is sustained primarily by material located further from the current collector, reducing the amount of available active material for continued intercalation. These effects lead to increased overpotential between pulses and limited capacity retention, even after the electrode has undergone a rest period.

In contrast, the flat voltage model predicts complete relaxation of the concentration profile, similar to what is observed in solid solution materials (Fig. 8c). Following the resting period, the homogeneous electrode can efficiently sustain the next pulse by utilizing the entire electrode volume, ultimately artificially increasing the delivered capacity. These properties suggest the physically consistent non-monotonic OCP should be regarded as the best solution for simulating phase-separating materials. The ability to reproduce the features of a GITT protocol makes this method suitable for intermittent scenarios, such as dynamic driving cycles, where current frequently alternates between charge and discharge, and rest periods are prolonged.

Moreover, it can naturally reproduce the voltage hysteresis without needing empirical algorithms (Fig. 9) and explain its

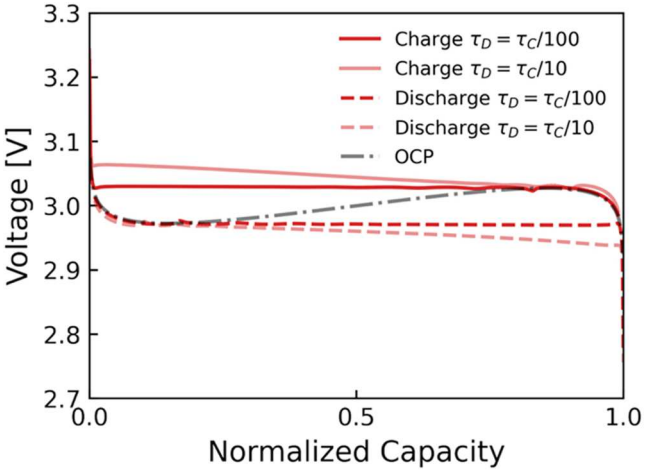

Figure 9. Charge and discharge curves at negligible reaction limitation ($\tau_R = \tau_C/100$) at varying τ_D. The gray line shows the open circuit potential as function of normalized capacity, in this example the entire cyclable capacity is used. The red curves show the results of slow insertion (bottom dotted lines) and de-insertion (top continuous lines) during a slow (dis)charge (τ_D, $\tau_R \ll \tau_C$).

features. Specifically, the apparent flat OCPs results from the multi-particle ensemble quickly reacting and equilibrating with the total system voltage, in line with theoretical predictions.[19] However,

the obtained low-rate voltage profile is not exactly a flat plateau, but it possesses a slight slope. In the case considered by this study, this is originating from the reaction front moving further way from the separator and thus, like in the GITT case, requiring higher overpotentials to react. Similar effects can be seen in case of thin electrodes with a wide particle size distributions, where the system sequentially react with particles of increasing sizes.[21] In both cases the experimental OCPs, even if obtained applying close-to-zero currents, would show an overpotential buildup resulting in monotonically sloping OCPs and would not be suitable for a physically consistent simulation of phase-separating materials.

Discussion and Conclusion

This work demonstrates the critical influence of open-circuit potential (OCP) characteristics on electrode dynamics, particularly in case of thick electrode composed by phase-separating nanoparticles. Compared to an electrode composed of solid solution nanoparticles —characterized by a monotonically decreasing OCP—a phase-separating material, with a non-monotonic OCP, exhibits drastically different electrolyte and solid concentration dynamics. By solely focusing on a transport limited electrode, we have shown how, aside from the differences in intra-particle dynamics,[7,10,26,28] these systems are also more susceptible to transport-induced limitations due to highly localized reactions, which accelerate electrolyte depletion. During insertion, the phase-separating electrode develops distinct inserted and depleted zones, a division that persists even when the current is stopped and the electrode is allowed to rest under open-circuit conditions. This effect manifests as an overpotential buildup during successive pulses in a GITT protocol, leading to a reduction in capacity retention that scales with the miscibility gap. Further studies should focus on the effect this phenomenon on more complex dynamic protocols. Additionally, while improvements in electrolyte diffusion enhance capacity retention and utilization across all materials, improvements in reaction kinetics negatively impact phase-separating materials by further increasing localized reactions.

We also evaluated the non-monotonic OCP approximation to the conventional flat OCP commonly used to simulate phase-separating materials such as LFP. While the two approaches yield similar voltage responses under constant current conditions, the GITT protocol reveals key differences. The flat OCP fails to capture internal phase separation dynamics, allowing for an unphysical relaxation of the solid concentration. This discrepancy carries significant implications for modeling dynamic cycling behavior—only non-monotonic OCPs accurately preserve path dependencies, charge-discharge hysteresis, and localized reaction evolution.

The results presented in this work are based on an idealized electrode composed of perfectly connected nanoparticles with negligible diffusion limitations. However, real battery electrodes exhibit additional complexities, such as diffusion-limited particles,[7,10,12,13,28] broad particle size distributions,[20] electron transport limitations,[32,33,50] and heterogenous porosity,[41] hierarchical structures,[11,40,51] contact losses,[52] mechanical effects,[53,54] etc.; all of which can mitigate the degree of reaction localization observed in this study. Moreover, the electrolyte dynamics can be better expressed using concentrated solution theory[35,36,42,43,55] and the reaction rate can be calculated by means of coupled ion-electron transfer theory.[56] The consequences of OCP monotonicity can also be investigated in realistic cell formats, observing how heat generation is affected.[57] Nonetheless, our findings emphasize the importance of implementing physically consistent, non-monotonic OCPs for phase-separating materials. The incorporation of this approach does not require substantial modifications to existing models[36,42,45] and retains computational efficiency comparable to the flat OCP method. Conversely, neglecting this feature may result in inaccurate predictions of dynamic cycling performance, lithium plating, and heterogeneous reaction distributions in large-format cells. Future efforts in electrode modeling and engineering for phase-separating materials should compare the results of physically consistent and simplified approaches before employing reduced-order models. For example, if the material consists of nanoparticles with negligible diffusion limitations and a fast simulation is required, a homogeneous one-dimensional porous electrode model may be more suitable than a single-particle model.[42,55] This framework is, therefore, essential for advancing the understanding of both existing and novel materials, providing critical insights necessary for the design, optimization, and modeling of phase-separating materials in next-generation energy storage systems.

Acknowledgments

P. O. and M. W. acknowledge the support of Shell Global Solutions International B. V.; A. V. acknowledge the Netherlands Organization for Scientific Research (NWO) under the VENI grant nr 18123.

Code Availability

The code needed to replicate the model's results is included as part of the supporting material.

ORCID

Pierfrancesco Ombrini https://orcid.org/0009-0004-0494-1403
Alexandros Vasileiadis https://orcid.org/0000-0001-9761-7936
Marnix Wagemaker https://orcid.org/0000-0003-3851-1044

References

1. J. M. Reniers, G. Mulder, and D. A. Howey, "Unlocking extra value from grid batteries using advanced models." *J. Power Sources*, **487**, 229355 (2021).
2. S. Kench, I. Squires, A. Dahari, F. Brosa Planella, S. A. Roberts, and S. J. Cooper, "Li-ion battery design through microstructural optimization using generative AI." *Matter*, S2590238524004466 (2024).
3. J. Park et al., "Fictitious phase separation in Li layered oxides driven by electro-autocatalysis." *Nat. Mater.*, **20**, 991 (2021).
4. R. Malik, A. Abdellahi, and G. Ceder, "A critical review of the li insertion mechanisms in $LiFePO_4$ electrodes." *J. Electrochem. Soc.*, **160**, A3179 (2013).
5. D. A. Cogswell and M. Z. Bazant, "Coherency strain and the kinetics of phase separation in $LiFePO_4$ nanoparticles." *ACS Nano*, **6**, 2215 (2012).
6. D. A. Cogswell and M. Z. Bazant, "Size-dependent phase morphologies in $LiFePO_4$ battery particles." *Electrochem. Commun.*, **95**, 33 (2018).
7. P. Ombrini, Q. Wang, A. Vasileiadis, F. Wu, Z. Gao, X. Hu, M. Van Hulzen, B. Li, C. Zhao, and M. Wagemaker, "Kinetically induced memory effect in Li-ion batteries." *EES Batter*, **1**, 437 (2025).
8. P. Ombrini, M. Z. Bazant, M. Wagemaker, and A. Vasileiadis, "Thermodynamics of multi-sublattice battery active materials: From an extended regular solution theory to a phase-field model of $LiMn_yFe_{1-y}PO_4$." *NPJ Comput. Mater.*, **9**, 148 (2023).
9. I. Timrov, F. Aquilante, M. Cococcioni, and N. Marzari, "Accurate electronic properties and intercalation voltages of olivine-type Li-ion cathode materials from extended hubbard functionals." *PRX Energy*, **1**, 033003 (2022).
10. A. Vasileiadis, N. J. J. de Klerk, R. B. Smith, S. Ganapathy, P. P. R. M. L. Harks, M. Z. Bazant, and M. Wagemaker, "Toward optimal performance and in-depth understanding of spinel $Li_4Ti_5O_{12}$ electrodes through phase field modeling." *Adv. Funct. Mater.*, **28**, 1705992 (2018).
11. H. Lian and M. Z. Bazant, "Modeling lithium plating onset on porous graphite electrodes under fast charging with hierarchical multiphase porous electrode theory." *J. Electrochem. Soc.*, **171**, 010526 (2024).
12. R. B. Smith, E. Khoo, and M. Z. Bazant, "Intercalation kinetics in multiphase-layered materials." *J. Phys. Chem. C*, **121**, 12505 (2017).
13. X. Lu et al., "Multiscale dynamics of charging and plating in graphite electrodes coupling operando microscopy and phase-field modelling." *Nat. Commun.*, **14**, 5127 (2023).
14. S. Park, Z. Wang, Z. Deng, I. Moog, P. Canepa, F. Fauth, D. Carlier, L. Croguennec, C. Masquelier, and J.-N. Chotard, "Crystal structure of $Na_2V_2(PO_4)_3$, an intriguing phase spotted in the $Na_3V_2(PO_4)_3$–$Na_1V_2(PO_4)_3$ system." *Chem. Mater.*, **34**, 451 (2022).
15. Y. Xiao et al., "Prussian blue analogues for sodium-ion battery cathodes: A review of mechanistic insights, current challenges, and future pathways." *Small*, 2401957 (2024).
16. H. Zhao et al., "Learning heterogeneous reaction kinetics from X-ray videos pixel by pixel." *Nature*, **621**, 289 (2023).
17. P. Bai, D. A. Cogswell, and M. Z. Bazant, "Suppression of phase separation in $LiFePO_4$ nanoparticles during battery discharge." *Nano Lett.*, **11**, 4890 (2011).
18. T. Katrašnik, J. Moškon, K. Zelič, I. Mele, F. Ruiz-Zepeda, and M. Gaberšček, "Entering voltage hysteresis in phase-separating materials: Revealing the electrochemical signature of the intraparticle phase-separated state." *Adv. Mater.*, **35**, 2210937 (2023).
19. W. Dreyer, J. Jamnik, C. Guhlke, R. Huth, J. Moškon, and M. Gaberšček, "The thermodynamic origin of hysteresis in insertion batteries." *Nat. Mater.*, **9**, 448 (2010).

20. Y. Li et al., "Current-induced transition from particle-by-particle to concurrent intercalation in phase-separating battery electrodes." *Nat. Mater.*, **13**, 1149 (2014).
21. T. R. Ferguson and M. Z. Bazant, "Phase transformation dynamics in porous battery electrodes." *Electrochim. Acta*, **146**, 89 (2014).
22. D. Fraggedakis, N. Nadkarni, T. Gao, T. Zhou, Y. Zhang, Y. Han, R. M. Stephens, Y. Shao-Horn, and M. Z. Bazant, "A scaling law to determine phase morphologies during ion intercalation." *Energy Environ. Sci.*, **13**, 2142 (2020).
23. H. D. Deng et al., "Correlative image learning of chemo-mechanics in phase-transforming solids." *Nat. Mater.*, **21**, 547 (2022).
24. S. Daubner, P. G. Kubendran Amos, E. Schoof, J. Santoki, D. Schneider, and B. Nestler, "Multiphase-field modeling of spinodal decomposition during intercalation in an Allen-Cahn framework." *Phys. Rev. Mater.*, **5**, 035406 (2021).
25. M. Rykner and M. Chandesris, "Free energy model for lithium intercalation in graphite: Focusing on the coupling with graphene stacking sequence." *J. Phys. Chem. C*, **126**, 5457 (2022).
26. Y. Zeng and M. Z. Bazant, "Cahn-hilliard reaction model for isotropic Li-ion battery particles." *MRS Proc.*, **1542**, mrss13-1542-g02-01 (2013).
27. T. Gao, Y. Han, D. Fraggedakis, S. Das, T. Zhou, C.-N. Yeh, S. Xu, W. C. Chueh, J. Li, and M. Z. Bazant, "Interplay of lithium intercalation and plating on a single graphite particle." *Joule*, **5**, 393 (2021).
28. M. Lagnoni and A. Bertei, "Electrochemical diffusion signatures of solid-solution and phase-separating active materials in Li-ion batteries." *J. Phys.: Energy*, **7**, 035024 (2025).
29. D. Zhuang and M. Z. Bazant, "Scaling analysis of mosaic phase separation in Li-ion batteries." *Phys. Rev. E*, **110**, 064142 (2024).
30. Z. Li et al., "Probing the effect of electrode thermodynamics on reaction heterogeneity in thick battery electrodes." *Adv. Mater.*, 2502299 (2025).
31. Y. Zhang, Z. Yang, and C. Tian, "Probing and quantifying cathode charge heterogeneity in Li ion batteries." *J. Mater. Chem. A*, **7**, 23628 (2019).
32. Y. Li et al., "Effects of particle size, electronic connectivity, and incoherent nanoscale domains on the sequence of lithiation in $LiFePO_4$ porous electrodes." *Adv. Mater.*, **27**, 6591 (2015).
33. A. R. Iarchuk, V. A. Nikitina, E. A. Karpushkin, V. G. Sergeyev, E. V. Antipov, K. J. Stevenson, and A. M. Abakumov, "Influence of carbon coating on intercalation kinetics and transport properties of $LiFePO_4$." *Chem. Electro. Chem.*, **6**, 5090 (2019).
34. E. C. Tredenick, A. M. Boyce, S. Wheeler, J. Li, Y. Sun, R. Drummond, S. R. Duncan, P. S. Grant, and P. R. Shearing, "Bridging the gap between microstructurally resolved computed tomography-based and homogenised Doyle-Fuller-Newman models for lithium-ion batteries." *J. Electrochem. Soc.*, **172**, 030503 (2025).
35. R. B. Smith and M. Z. Bazant, "Multiphase porous electrode theory." *J. Electrochem. Soc.*, **164**, E3291 (2017).
36. T. R. Ferguson and M. Z. Bazant, "Nonequilibrium thermodynamics of porous electrodes." *J. Electrochem. Soc.*, **159**, A1967 (2012).
37. K. Zelič and T. Katrašnik, "Thermodynamically consistent derivation of chemical potential of a battery solid particle from the regular solution theory applied to $LiFePO_4$." *Sci. Rep.*, **9**, 2123 (2019).
38. E. Prada, D. Di Domenico, Y. Creff, J. Bernard, V. Sauvant-Moynot, and F. Huet, "A simplified electrochemical and thermal aging model of $LiFePO_4$-graphite Li-ion batteries: power and capacity fade simulations." *J. Electrochem. Soc.*, **160**, A616 (2013).
39. D. Wycisk, M. Oldenburger, M. G. Stoye, T. Mrkonjic, and A. Latz, "Modified Plett-model for modeling voltage hysteresis in lithium-ion cells." *J. Energy Storage*, **52**, 105016 (2022).
40. O. Birkholz and M. Kamlah, "Electrochemical modeling of hierarchically structured lithium-ion battery electrodes." *Energy Technol.*, **9**, 2000910 (2021).
41. P. Karanth, M. Weijers, P. Ombrini, D. Ripepi, F. Ooms, and F. M. Mulder, "A phase inversion strategy for low-tortuosity and ultrahigh-mass-loading nickel-rich layered oxide electrodes." *Cell Rep. Phys. Sci.*, 101972 (2024).
42. F. Brosa Planella et al., "A continuum of physics-based lithium-ion battery models reviewed." *Prog. Energy*, **4**, 042003 (2022).
43. M. Lagnoni, C. Nicolella, and A. Bertei, "Comparison of electrolyte transport modelling in lithium-ion batteries: concentrated solution theory vs generalized Nernst-Planck model." *J. Electrochem. Soc.*, **169**, 020570 (2022).
44. A. M. Bizeray, D. A. Howey, and C. W. Monroe, "Resolving a discrepancy in diffusion potentials, with a case study for Li-ion batteries." *J. Electrochem. Soc.*, **163**, E223 (2016).
45. V. Sulzer, S. G. Marquis, R. Timms, M. Robinson, and S. J. Chapman, "Python battery mathematical modelling (PyBaMM)." *J. Open Res. Softw.*, **9**, 14 (2021).
46. J. A. E. Andersson, J. Gillis, G. Horn, J. B. Rawlings, and M. Diehl, "CasADi: A software framework for nonlinear optimization and optimal control." *Math. Program. Comput.*, **11**, 1 (2019).
47. Delft University of Technology W. Haverkort, *Electrolysers, Fuel Cells and Batteries* (TU Delft OPEN Publishing) (2024), https://books.open.tudelft.nl/home/catalog/book/176.
48. V. Srinivasan and J. Newman, "Existence of path-dependence in the $LiFePO_4$ electrode." *Electrochem. Solid-State Lett.*, **9**, A110 (2006).
49. H. D. Deng, N. Jin, P. M. Attia, K. Lim, S. D. Kang, N. Kapate, H. Zhao, Y. Li, M. Z. Bazant, and W. C. Chueh, "Beyond constant current: origin of pulse-induced activation in phase-transforming battery electrodes." *ACS Nano*, **18**, 2210 (2024).
50. P. Ombrini et al., "Modeling single-crystal electrodes as a network of primary particles." *ChemRxiv.* (2025).
51. S. Daubner, M. Weichel, M. Reder, D. Schneider, Q. Huang, A. E. Cohen, M. Z. Bazant, and B. Nestler, "Simulation of intercalation and phase transitions in nano-porous, polycrystalline agglomerates." *NPJ Comput. Mater.*, **11**, 211 (2025).
52. T. K. Schwietert, P. Ombrini, L. S. Ootes, L. Oostrum, V. Azizi, D. Cogswell, J. Zhu, M. Z. Bazant, M. Wagemaker, and A. Vasileiadis, "Phase-field computational framework for addressing challenges in solid-state batteries." *PRX Energy*, **2**, 033014 (2023).
53. G. Ipers, J. Jiao, S. Pathak, R. Fang, M. D. Berliner, W. Li, W. Li, R. D. Braatz, M. Z. Bazant, and J. Zhu, "Rapid simulation of electro-chemo-mechanical deformation of Li-ion batteries based on porous electrode theory." *J. Electrochem. Soc.*, **171**, 050557 (2024).
54. W. Ai, L. Kraft, J. Sturm, A. Jossen, and B. Wu, "Electrochemical thermal-mechanical modelling of stress inhomogeneity in lithium-ion pouch cells." *J. Electrochem. Soc.*, **167**, 013512 (2019).
55. S. G. Marquis, V. Sulzer, R. Timms, C. P. Please, and S. J. Chapman, "An asymptotic derivation of a single particle model with electrolyte." *J. Electrochem. Soc.*, **166**, A3693 (2019).
56. M. Z. Bazant, "Unified quantum theory of electrochemical kinetics by coupled ion-electron transfer." *Faraday Discuss*, **246**, 60 (2023).
57. K. O'Regan, F. Brosa Planella, W. D. Widanage, and E. Kendrick, "Thermal-electrochemical parameters of a high energy lithium-ion cylindrical battery." *Electrochim. Acta*, **425**, 140700 (2022).